
Article:
Kearney, S.A. orcid.org/0000-0002-1895-502X, McLuckie, B., Webb, K. et al. (7 more authors) (2020) Effects of plutonium dioxide encapsulation on the physico-chemical development of Portland cement blended grouts. Journal of Nuclear Materials, 530. 151960. ISSN 0022-3115

https://doi.org/10.1016/j.jnucmat.2019.151960

Effects of plutonium dioxide encapsulation on the physico-chemical development of Portland cement blended grouts.

Sarah A. Kearney[1], Bliss McLuckie[2], Kevin Webb[2], Robin Orr[2], Ian A. Vatter[2], Antonia S Yorkshire[1], Claire L. Corkhill[1], Martin Hayes[2], Michael J. Angus[2], and John L. Provis*[1]

[1] NucleUS Immobilisation Science Laboratory, Department of Materials Science and Engineering, University of Sheffield, Sheffield, S1 3JD, United Kingdom
[2] National Nuclear Laboratory, Sellafield, Seascale, Cumbria CA20 1PG, United Kingdom
*Correpsonding author: J.provis@sheffield.ac.uk

Keywords: Cement encapsulation, Plutonium, radiolysis, microstructural and phase assemblage changes.

Highlights:

- PuO_2 was encapsulated in BFS / PFA blended cements used for nuclear waste disposal
- Cellulose was added to the systems to investigate the effects of organics.
- No large scale microstructural defects were observed and good physical contact between the PuO_2 and grout was seen.
- Changes to the phase assemblage were noted in BFS containing grouts.
- Radiolytic gas evolution was consistent with expectations, with increased values observed for samples containing cellulose.

Declarations of interest: none

Abstract

The effects of alpha radiation on cementitious systems used for nuclear waste encapsulation, and the subsequent physico-chemical properties, have been subject to limited investigation comparative to the effects of gamma and neutron irradiations. This paper outlines an assessment of the impact of PuO_2 incorporation on the bulk characteristics of BFS and PFA blended Portland cements, with specific focus on the microstructure, phase assemblage and the radiolysis of pore water. Cellulose was also added to the cements to investigate the effects of organics on these systems. Characterisation of the bulk phase assemblage and microstructure were completed using optical and scanning electron microscopy (SEM), x-ray diffraction (XRD), and thermogravimetric analysis (TGA). Gas evolution was measured to determine the radiolytic breakdown of pore solution. In all samples the PuO_2 appeared well encapsulated, with good physical contact to the cement grout and no large scale defects observed. Pu-containing hydrates were not observed, but PuO_2 containing BFS based systems showed variations in the ratio of sulfate-containing phases, with increased ettringite observed. Gas evolution results were consistent with expectations based on likely radiation deposition, and increased $G(H_2)$ values were observed for cellulose containing samples. The findings of this study suggest the investigated cements are suitable encapsulants matrices for wastes containing PuO_2.

Graphical Abstract

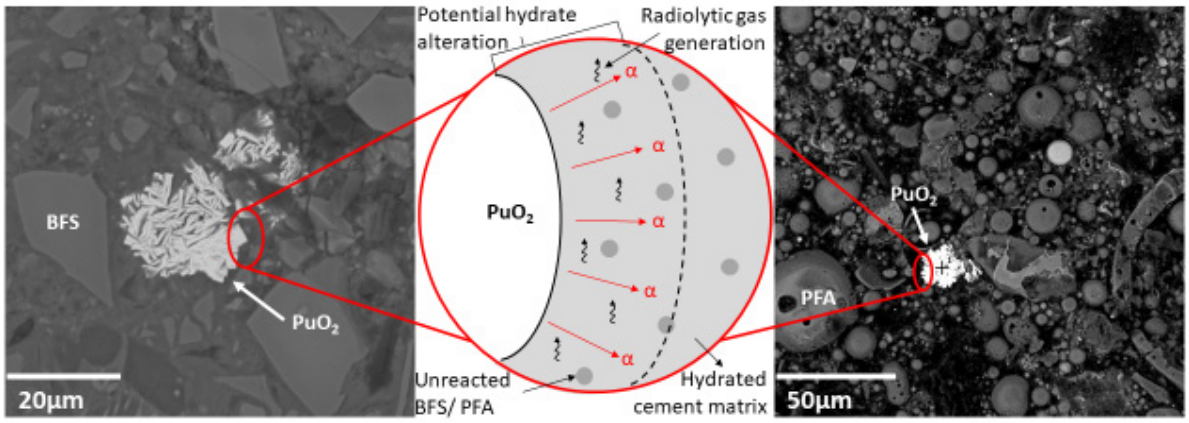

1. Introduction

Encapsulation in cementitious grout is the baseline treatment strategy for the majority of the UK's Intermediate Level Waste (ILW) [1]. The grouts, based on Portland cement (PC), are tailored for specific suitability to the waste materials by the addition of supplementary cementitious materials (SCMs) including blast furnace slag (BFS) and pulverised fuel ash (PFA).

Plutonium contaminated materials (PCM) are a sub category of ILW that includes process equipment and materials used in Pu finishing and mixed oxide (MOX) fuel pellets production, in addition to Pu-contaminated high efficiency particulate in air (HEPA) filters [2]. PCM waste is initially stored in 200 L drums prior to high force compaction, creating a puck that is encapsulated within a 500 L drum using a PFA:PC grout. These drums may contain up to 260 g Pu and U-235, combined. The initial mean specific activity of PCM drums produced up to 2016 is ~1 TBq/m^3 alpha and 12.1 TBq/m^3 beta / gamma [3]. Over time, alpha decay leads to the ingrowth of actinide daughters, including isotopes of americium and uranium. Plutonium, within fuel residues, is also expected to reside in BFS:PC grouts used to encapsulate Magnox fuel swarf. These canisters, 500 L in size, have a mean specific activity of ~175 TBq/m^3, of which ~18 TBq/m^3 is from Pu isotopes [4,5]. The interface between radionuclide species and cement materials, which may be highly localised, is of specific interest, since these areas can be subjected to high levels of ionising radiation throughout their service life. As such, it is important to build an understanding of how Pu, ranging from soluble nitrates to solid oxides, interacts with cement minerals.

Firstly, one must consider the role of radiation within the Pu-cement system. Two key processes are likely to induce reactions within cement materials upon irradiation: (i) radiolysis of pore fluid; and (ii) direct impact of alpha and alpha-recoil particles. Radiolytic decomposition of water generates H_2, e^-_{aq}, H, OH^-, H_2O, H^+, OH and H_2O_2 as primary products [6]; generation of $H_{2(g)}$ may pressurise the wasteform, leading to cracking of the cement and creation of a potential explosion risk [7,8]. In grout systems containing BFS, the oxidation of sulfide to sulfate is of particular concern since internal sulfate attack may occur [9,10]. This is analogous to external sulfate attack, where ettringite forms at the expense of monosulfate and portlandite in an expansive nature, causing damage [11,12].

Volumetric expansion is widely reported to result from direct impact of alpha- and alpha-recoil particles within crystalline phases [13,14]. The production of damage zones, typically highly localised, will affect cement microstructure and cause expansion, which may impact physico-chemical properties; hypothetically, this may manifest as a layer of altered hydrates in alpha deposition zones, similar to radiohalos seen in natural minerals [15–18]. The localised absorption of energy around alpha

emitting species could hypothetically increase pressurisation within closed porosity compared to an equivalent dose from gamma exposure. This increased pressurisation may lead to cracking, chipping, spallation and reduction in compressive strength becoming more prevalent.

One further consideration is the potential influence of radiolytic effects on degradation of the wasteform itself. For example, the degradation of organic materials such as cellulose, which was a significant component of PCM wastes prior to the 1980s, can produce gaseous products and soluble organic compounds that may result in swelling of the cement and increased radionuclide solubility, respectively [19,20].

Given the potential for radiation effects in Pu-containing cement grouts, this study aims to assess the impacts of alpha radiation, arising from PuO_2, on the hydration and physico-chemical properties of BFS and PFA:PC blended cement systems relevant to nuclear waste encapsulation. These results can be used to enhance understanding of ageing processes for existing encapsulated products and to support development of waste storage and disposal safety cases.

2. Materials and Methods

Portland cement conforming to Sellafield Ltd (SL) specification was supplied by Hanson Cement as Ketton coarse ground PC. BFS conforming to SL specification was also obtained from Hanson Cement as Scunthorpe GGBS blended with Calumite® (a coarse ground material produced from blast furnace slag) in a 70:30 weight ratio. PFA was from the CEMEX Drax plant and conformed to BS EN 450-1 as well as the SL specification regarding performance in a pre-prepared grout mix [21]. Oxide composition and other available details of the powders are given in Table 1.

Table 1 Major constituents of raw materials determined via X-ray fluorescence (XRF).

Oxide (wt.%)	PC	BFS	PFA
SiO_2	21.6	36.1	52.9
Al_2O_3	5.1	11.4	24.8
Fe_2O_3	2.6	0.4	8.4
CaO	64.9	39.4	2.5
K_2O	0.8	0.7	3.1
MgO	1.0	8.4	1.6
Na_2O	0.2	0.4	1.2
TiO_2	0.4	0.9	0.9
Mn_2O_3		0.6	0.1
MnO	0.1	0.6	
SO_3	2.6	-	0.1
S^{2-}	-	0.8	
Cl^-	0.1	0.0	0.1
$SiO_2+Al_2O_3+Fe_2O_3$	-	-	84.6
Glass count	-	97	
Surface area	-	357 $m^2.kg^{-1}$‡	9.1 %*
LOI	≤1.5 %†	-	≤7 %†

‡Blaine fineness

*Residue on a 0.045 mm mesh sieve

†Limits specified by the SL powder specification

Plutonium dioxide (PuO_2) was obtained from the Sellafield Ltd. Magnox reprocessing plant. PuO_2 is manufactured by precipitation of plutonium(IV)oxalate from plutonium nitrate, which is washed and

calcined at 650 °C. The specific surface area of the PuO_2, determined by BET analysis using nitrogen as the adsorbate, was 11.8 $m^2\ g^{-1}$. The isotopic composition is given in Table 2. The α particle dose rate was $2.8x10^{10}$ MeV s^{-1} $g(Pu)^{-1}$. At the PuO_2 loading used in these experiments (0.5 wt%) the dose rate to the sample was ~72 Gy h^{-1}.

Table 2 Plutonium and americium isotopic composition of PuO_2 accounting for ^{241}Am in-growth

	^{238}Pu	^{239}Pu	^{240}Pu	^{241}Pu	^{242}Pu	^{241}Am
Wt. fraction heavy metal	0.0027	0.72	0.23	0.032	0.0011	$4.90x10^{-3}$

Samples were prepared with 5 wt % microgranular cellulose to simulate organic containing waste streams, as degradation products can form soluble actinide complexes. Grout formulations representative of those used for encapsulation of ILW were prepared according to Table 3.

Table 3 Grout formulations

Samples	Powder blend	Powder ratio	*w/s* ratio	Cellulose* (wt%)	PuO_2* (wt%)
BFS:PC	BFS:PC	3.44:1	0.35	-	-
BFS:PC + Pu	BFS:PC	3.44:1	0.35	-	0.50
BFS:PC + C	BFS:PC	3.44:1	0.35	5.0	-
BFS:PC + C + Pu	BFS:PC	3.44:1	0.35	5.0	0.50
PFA:PC	PFA:PC	3:1	0.43	-	-
PFA:PC + Pu	PFA:PC	3:1	0.43	-	0.51
PFA:PC + C	PFA:PC	3:1	0.43	5.0	-
PFA:PC + C + Pu	PFA:PC	3:1	0.43	5.0	0.49

*Expressed as a weight percentage of the grout mix mass

2.1 Sample synthesis

Grouts were first prepared at room temperature in a non-radioactive laboratory using a method developed to assess powder properties for current intermediate level waste (ILW) encapsulation plant processes [21]. Cement precursors were added to deionised water while mixing (3L low-shear) over a period of 5 minutes, with PC added first, followed by another 5 minutes of mixing at low shear and then 10 minutes at 6000 rpm in a high shear mixer. Non-radioactive reference samples were prepared in ~1 cm^3 moulds. For formulations containing cellulose, cellulose powder was added by hand mixing to 100 g of cement paste. Within an α-radioactive glovebox, approximately 0.5 g PuO_2 was added to 100 g of cement paste (with or without cellulose) prior to mixing by hand and placing within ~1 cm^3 moulds. All samples were cured for 28 days in sealed bags with water to maintain high relative humidity, after which time they were de-moulded. The samples were then placed in vessels and covered with $Ca(OH)_2$-saturated water to control the pH and to prevent leaching of cement phases from the sample. The vessels were sealed to minimise atmospheric carbonation effects.

2.2 Hydrogen yield measurements

After one month of hydration, the yield of hydrogen from PuO_2 containing samples was measured. Ten cubes of a single formulation were placed in a sealed glass vessel, which was fitted with a valve to allow periodic sampling using a gas tight syringe. Cement cubes were maintained under calcium hydroxide saturated water during the measurements. After removing each sample of gas from the vessel, a measured volume of air was immediately returned to maintain approximately atmospheric pressure in the vessel. The hydrogen concentration was determined using a Varian 490 micro-GC operating with a Molsieve 5A column, argon carrier gas and calibrated with a 102 ppm standard. The cumulative hydrogen production was calculated from the hydrogen concentration in each sample, the

gas sample volume, air volume returned and vessel headspace volume. Gas samples were generally taken daily. After six to eight days of measurements, the vessel was fully vented to remove all the hydrogen present and measurements of the accumulated hydrogen restarted. Typically two or three sets of measurements of hydrogen accumulation were made over a period of up to 24 days.

2.3 Sample characterisation

Characterisation of samples was performed after approximately one year of curing. Control samples were provided to the University of Sheffield to enable characterisation of the phase assemblage and microstructure, whilst the PuO_2 containing samples remained at the NNL active facilities to allow concurrent analysis. Analytical protocols were dictated by the constraints imposed of handling PuO_2 samples under local health and safety requirements. As a result, some variation from typical preparation methods was required. Hydration of the samples was not halted prior to any analysis, powders were crushed several days prior to analysis and stored under vacuum in a desiccator, and the materials did not undergo sieving before XRD and TGA testing. All preparation and subsequent storage occurred at room temperature. Despite concurrent analysis, due to alpha handling protocols, equipment location, and local variations in storage conditions between the radioactive and non-radioactive samples in the period between preparation and analysis, atmospheric carbonation effects cannot be fully evaluated.

2.3.1 Non-radioactive Reference Samples

Upon receipt from NNL, non-radioactive reference samples were stored in a controlled environmental chamber at 20°C and 95% relative humidity. Prior to this, samples were stored as detailed in section 2.1. After removal from the curing solution, slices were cut and mounted in epoxy resin or crushed into a fine powder by hand using a pestle and mortar, during which time atmospheric carbonation may have occurred. Sample preparation and analysis was co-ordinated with NNL, and the samples were stored in a Parafilm® sealed jar inside a desiccator at room temperature until analysis was completed.

Mounted monolith samples were prepared for SEM analysis by successive grinding (240-1200 SiC grit papers) and polishing (6 µm - 0.25 µm) with diamond suspension. Following carbon coating, backscatter electron images were collected using a Hitachi TM3030 SEM with a 15 kV accelerating voltage and a working distance of 8.5 to 9 mm. Semi-quantitative chemical analysis by Energy Dispersive X-ray Spectroscopy (EDS) was completed using a Bruker Quantax 70 detector, and elemental mapping was completed for 10 minutes. For spot analysis, 150 points were manually chosen focussing on areas of C-A-S-H from 3 mapping areas taken at 1500 magnification with a spot size of 9.5 microns. C-A-S-H was targeted using the characteristic light grey colour identifiable in the matrix. Powder XRD analysis was performed using a Bruker D2 Phaser with Cu Kα radiation and a nickel filter, operating between 5° < 2θ < 60° with a step size of 0.02 °2θ. Thermogravimetic analysis (TGA) was completed using a Perkin Elmer Pyris 1 TGA 4000 in conjunction with a HPR-20 QIC Benchtop Gas Analyser System. Analysis was performed between 25 and 1000 °C, at a rate of 10 °C per minute, under a nitrogen atmosphere with a flow rate of 40 mL/minute. Free water loss was assessed as the percentage weight loss between 30 – 105°C. The amounts of portlandite and carbonate in the pastes were quantified from the weight loss between 400 to 500°C, and 550 to 800°C, respectively, using the tangential method [22] and calculated according to Eqns. (1) and (2):

$$Ca(OH)_2 = \frac{weight\ loss\ (Ca(OH)_2)}{100 - water\ loss\ _{(30-500°C)}} \times \frac{M_{Ca(OH)_2}}{M_{H_2O}} \quad (1)$$

$$CaCO_3 = \frac{weight\ loss\ (CaCO_3)}{100 - \text{CO loss}_{\ (30-800°C)}} \times \frac{M_{CaCO_3}}{M_{CO_2}} \quad (2)$$

where the portlandite and carbonate wt. % is expressed as percentage of the dry sample weight at 500°C and 800°C respectively, and M is the molar mass. The relative error of these measurements is ±5-10% [23].

2.3.2 PuO_2 Containing Samples

The PuO_2-containing samples were stored in glovebox facilities. No temperature controls were implemented in the glovebox. Samples were cut from the 1 cm^3 cubes for grinding and mounting for microscopy. Samples were ground by hand using a pestle and mortar inside the glovebox for XRD and TGA analysis. For SEM preparation, samples underwent successive grinding using 220 – 3 µm diamond suspensions with resin bonded diamond discs, followed by polishing using 1 µm - 0.25 µm diamond suspensions with alcohol based lubricant. Due to alpha handling protocols and equipment location, movement of the samples between laboratories was required for several of these stages increasing the overall preparation time. During this period the samples were stored in a glovebox. During transfer of samples for analysis atmospheric carbonation may have occurred.

The TGA characterisation was performed using a Seteram TGA 92-1800 installed in a plutonium active glovebox. Samples of 40 mg in an alumina crucible were analysed between 25 and 1000°C, at a rate of 10 °C per minute, under a nitrogen atmosphere with a flow rate of 40 mL/minute. The raw TG data were processed to produce the derivative weight loss using a Mathematica script based on Tikhonov regularization that calculates the first derivative via the second derivative [24], and a correction for the formation of condensation in equipment tubing during the initial hold temperature was applied. Quantities of $Ca(OH)_2$ and $CaCO_3$ were calculated using Eq. (1), (2). Variations in peak width and position are present between the PuO_2 containing and control results for all samples; this is likely the result of equipment differences.

XRD analysis was completed using a Bruker D8 ADVANCE with Cu Kα radiation operating between 5° < 2θ < 60° with a step size of 0.02 °2θ. The samples were mixed with Epofix resin and loaded into a polymethylmethacrylate (plexiglass) puck, giving rise to intense diffuse scattering in the background of all diffractograms. This was sealed using an additional layer of resin. The results were processed to subtract background, and this removed diffuse scatter associated with poorly crystalline hydrate phases and unreacted SCM. The data were subjected to an overall plot offset of -0.25° 2θ to correct for equipment drift. Whilst this was effective for 2θ > 23°, peak positions at low angles are slightly more variable, potentially due to the data processing that removed background scatter.

Bright and dark field optical microscopy was completed using a Leica DM1500 M inverted binocular microscope with 50x magnification, installed in a plutonium active glove box. Estimation of porosity was completing by inferring an arbitrary pore threshold from the dark field greyscale histogram using ImageJ software. SEM-BSE imaging was carried out using a Phenom ProX desktop instrument. The instrument has a backscatter electron detector for imaging at accelerating voltages of 5 – 15 kV and a magnification range of 80 – 130000x with a resolution of < 10 nm.

3. Characterisation results and discussion

3.1 Influence of PuO_2 on BFS:PC

3.1.1 Microstructural development

Figure 1 shows the development of a characteristic microstructure for BFS:PC grouts, displaying unhydrated cement clinker and BFS together with hydrate products including portlandite and AFm-type phases. Figure 2 shows a hydrated cement clinker grain and the surrounding matrix; textural

differences between the denser appearing inner product and the surrounding outer product forming the remaining matrix can be seen. EDX analysis shows distribution of aluminium throughout the matrix indicating substitution into C-S-H to form C-A-S-H [25,26]. Dark rims surrounding the BFS indicate hydration of the particle, forming a hydrotalcite-like product [27,28]. Residual iron from the BFS can be seen in the Fe mapping shown in Figure 2, as observed in other BFS containing cements [29]. High concentrations of sulfur are shown in Figure 2 which together with low Si content indicates high proportions of AFm-type phases in this region. Cracking was observed at a range of scales, thought to be the product of sample preparation rather than of curing.

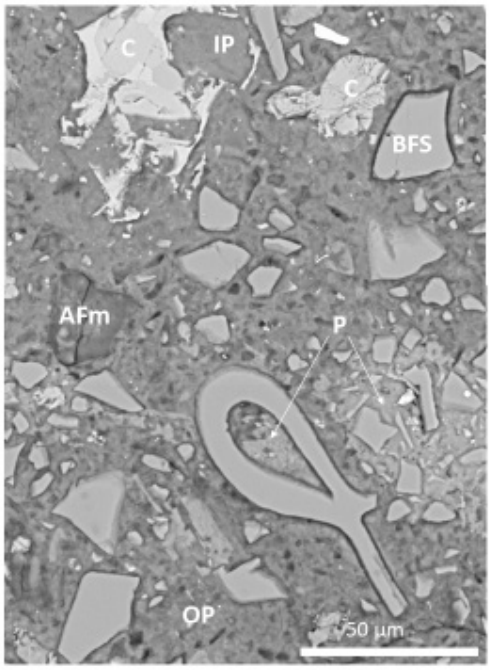

Figure 1 BSE micrograph of BFS:PC showing characteristic microstructural development and some identifiable phases: C: unreacted cement clinker, BFS: unreacted BFS (larger grains are Calumite®), AFm: monosulfoaluminate-type phase, P: Portlandite (lighter grey areas of matrix), IP: matrix inner product, OP: matrix outer product.

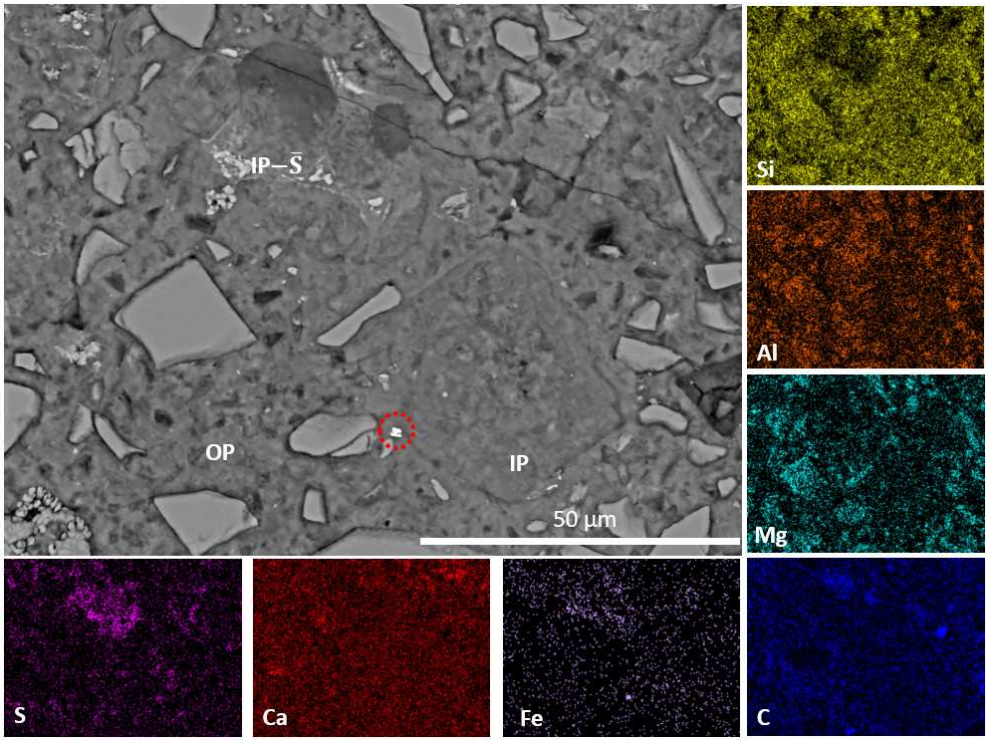

Figure 2 BSE micrograph and EDS analysis of BFS:PC grout showing a clinker grain which is almost fully hydrated. IP) inner product C-A-S-H, OP) outer product C-A-S-H and IP-S̄) S rich inner product – potential AFm formation. Residual Fe from BFS is highlighted by the dashed red circle.

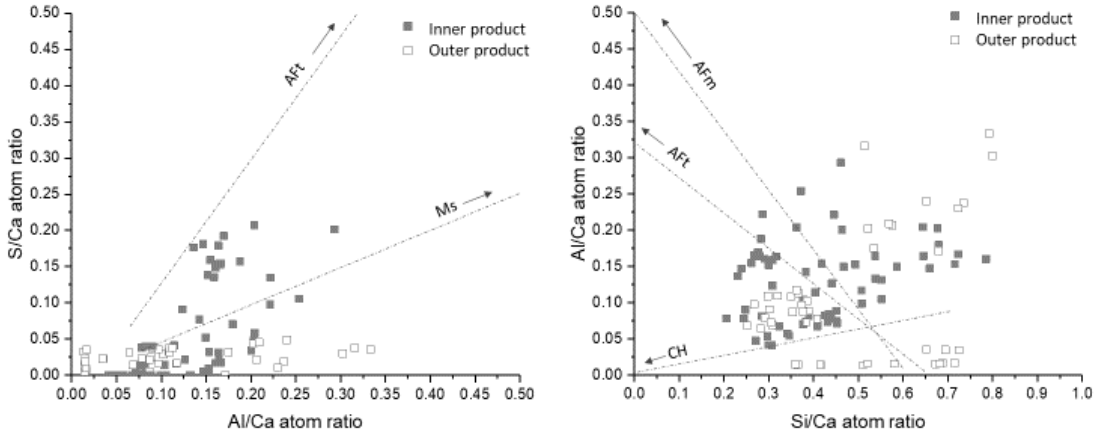

Figure 3 Atomic ratio plots from EDX spot analysis of areas IP, OP and IP-S̄) (shown in Figure 2) demonstrating the variations across the matrix.

Spot analyses from the BFS:PC samples were taken and ratio plots are shown in Figure 3. Due to intermixing of the hydrate phases results should not be treated as quantitative, but broad trends are provided such as lower Si/Ca ratio for the outer matrix product, and inner product areas containing higher proportions of sulfate containing phases.

The BFS:PC + Pu grouts display no large scale defects within the matrix (Figure 4). Large unreacted Calumite® particles are identifiable in the hydrate matrix and areas of red-brown coloration were noted, thought to represent ferrite rich hydrate zones although no SEM EDX has been completed. Porosity estimations from the thresholding of the dark field images using ImageJ was 3.63%.

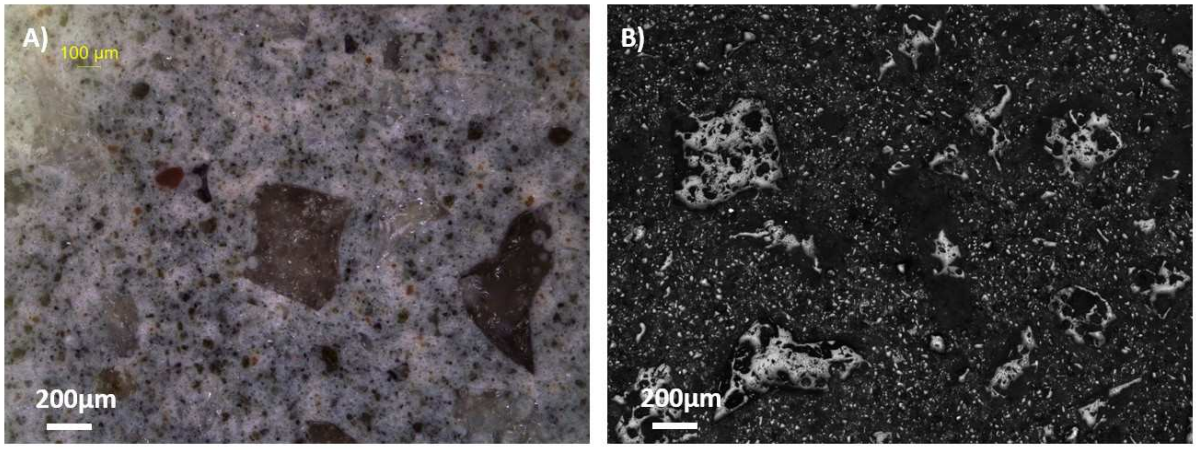

Figure 4 Optical images of BFS:PC + Pu cements. A) Bright field image, B) Dark field image

3.1.1.1 Effects of cellulose addition

The incorporation of cellulose powder does not appear to have had a significant impact on the microstructural development of the grout in the BFS:PC + C sample. Cracking in the cellulose is present, which may be due to sample preparation techniques together with cellulose degradation. There is some smudging evident at the outer boundaries of the encapsulated cellulose that may indicate greater decomposition of the cellulose material.

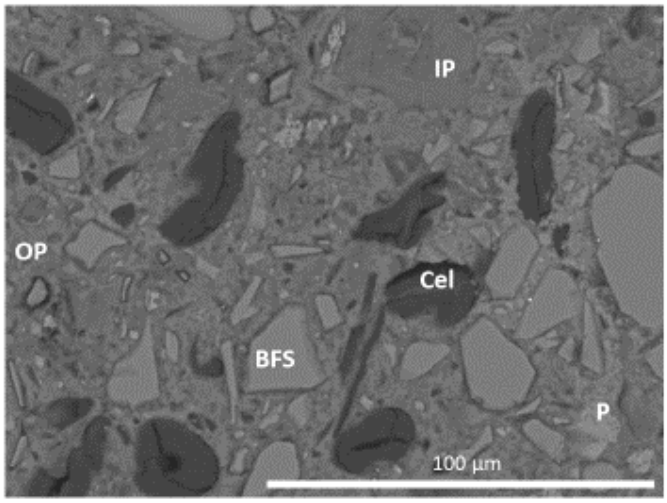

Figure 5 BSE micrograph of BFS:PC + C grout. Cel: cellulose powder, BFS: unreacted BFS (larger grains are Calumite®), P: Portlandite (lighter grey areas of matrix), IP: matrix inner product, OP: matrix outer product.

BFS:PC + C + Pu samples show similar textural development to BFS:PC + Pu samples, and no significant microstructural alteration noted – no large scale cracking was observed in the bulk matrix (Figure 6). Porosity was estimated to be 3.1%, using thresholding of the greyscale histogram of the dark field images.

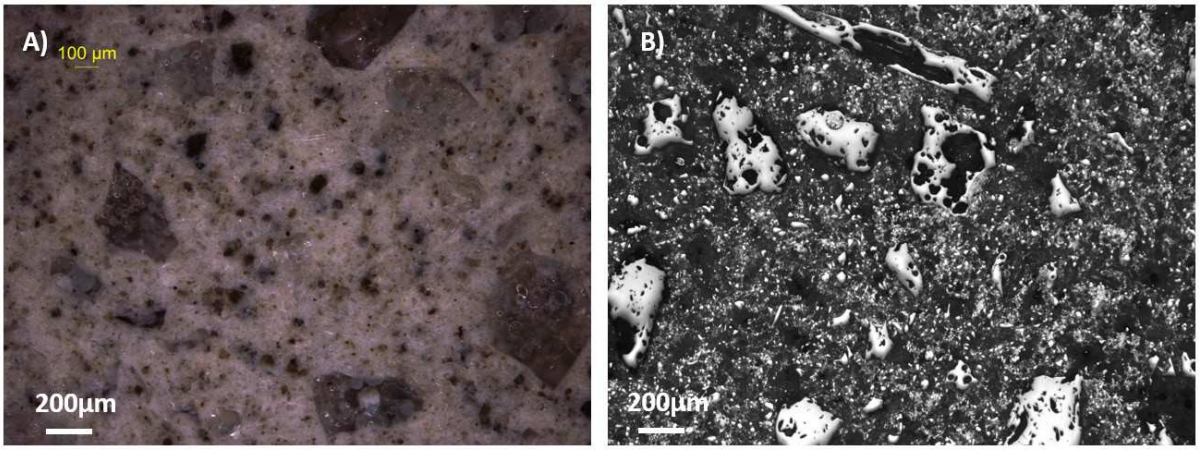

Figure 6 Optical images of BFS:PC + C + Pu cements. A) Bright field image, B) Dark field image

SEM investigation of the BFS:PC + C + Pu also showed no large scale defects in the matrix surrounding the PuO_2 particles, which appear to have been well encapsulated in the matrix (Figure 7). Limited investigation of the interface between the PuO_2 and the grout has been completed, however Figure 7 C) shows this area is of interest; label 1 indicates that good infilling of PuO_2 by the grout has been achieved around most of the particle, whilst label 2 shows a low contrast backscatter area which may be due to cellulose particles, or topographic differences that might be a result of a damaged zone [17]. Pervasive cracking was also not observed, indicating overpressure of the matrix through gas generation did not occur.

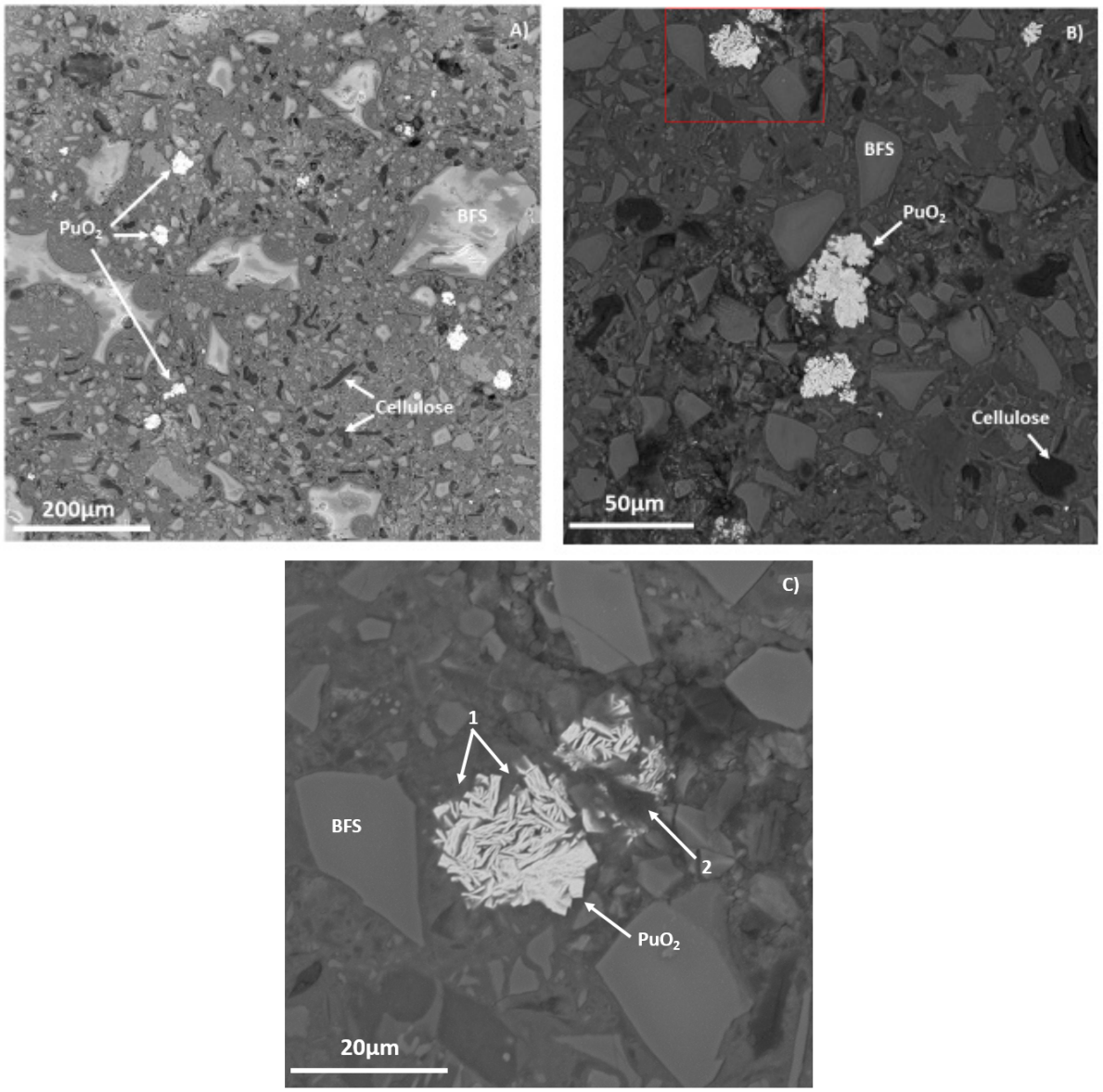

Figure 7 BFS:PC + C + Pu at increasing magnification levels in A), B) and C). Red zone in image B) shows PuO_2 particle shown in image C). Labels 1, 2, in image C) are expanded on in text.

3.1.2 Phase assemblage

The phase assemblage identified is typical of BFS:PC blended systems. XRD results display reflections attributed to ettringite (PDF#-41-1451), monosulfoaluminate (PDF#-83-1289), hemicarboaluminate (PDF#-014-0221), hydrotalcite (PDF#-14-0191), monocarboaluminate (PDF#-36-0377), portlandite (PDF#-04-0733), C-A-S-H, and calcite (PDF#-01-0837) together with unreacted belite (PDF#-29-0369) and BFS (attributed to the diffuse scatter at $25°<2\theta<35°$) are indicated in Figure 15. The peaks from the PuO_2 are shown by the light grey dashed lines.

Due to the background stripping analysis, the peak intensities and peak width cannot be used to quantitatively evaluate radiation induced variations in crystal structure. Qualitative evaluation of phase assemblage was completed by assessing the peak positions and intensity. Variation in the diffraction patterns was observed at low angles, where the peak associated with the [100] ettringite reflection had higher intensity in the BFS:PC + Pu sample. A slight shift in peak position was noted, however this is thought to be a product of the original peak offset having less impact at low angles

rather than substitution either of Fe for Al in the ettringite [30], or of a shift in the end member proportions of the AFm phases [31].

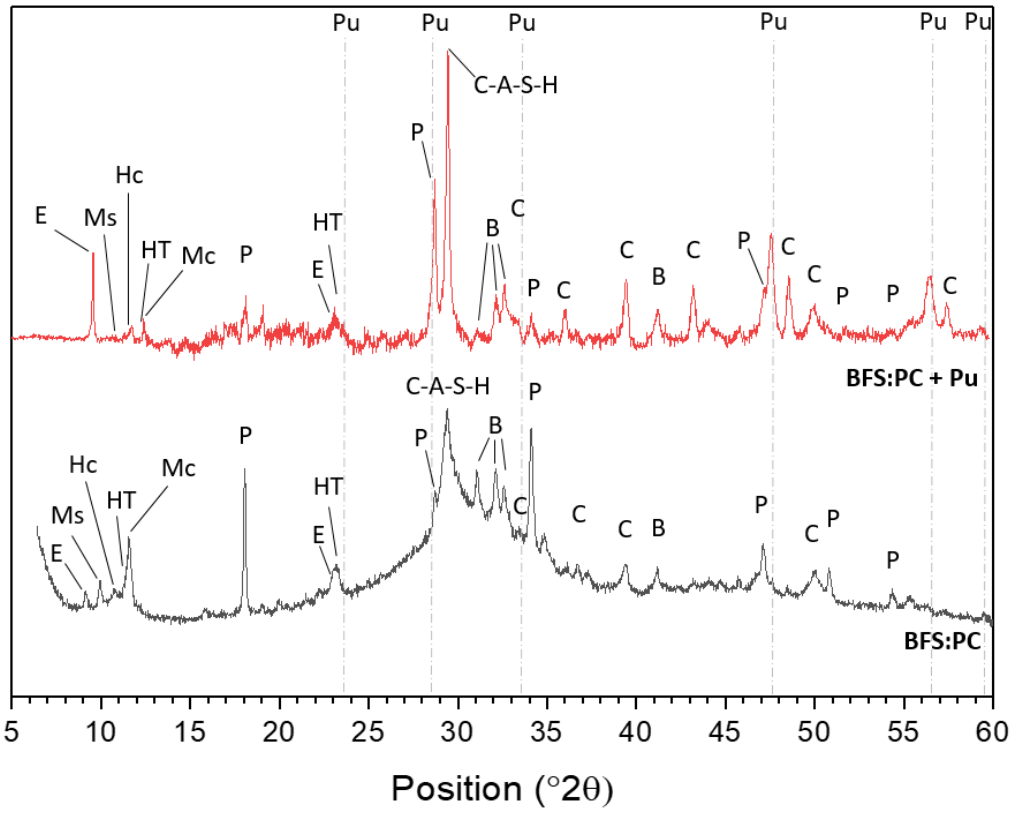

Figure 8 XRD data from BFS:PC and BFS:PC + Pu grouts. E: ettringite, Ms: monosulfoaluminate, Hc: hemicarboaluminate, HT: hydrotalcite, Mc: monocarboaluminate, P: portlandite, C-A-S-H: aluminium substituted calcium silicate hydrate, B: belite, C: calcite, Pu: PuO_2

The increase in peak intensity for ettringite comparative to the peaks for monosulfoaluminate (not present), monocarboaluminate, hydrotalcite, and hemicarboaluminate indicates an increase in the proportion of ettringite present in the BFS:PC + Pu sample. This increase may be the result of radiolytic induced oxidation of sulfide released from the BFS, as observed by Richardson et al. [9] in gamma irradiation studies. The presence of ettringite was not observed at the expense of monosulfoaluminate in that study, unlike the results shown here. The reduction in the peak intensities for the AFm phases (monosulfoaluminate, monocarboaluminate, hemicarboaluminate) in the diffraction patterns may indicate that the increase in sulfate content was sufficient to allow later age conversion back to ettringite. However, as AFm phases are partially XRD amorphous, comparison of peak intensities may be misleading and overlapping dehydration temperatures for these phases in TGA offers no further clarification [22,32].

The sulfate content of the BFS:PC systems will only increase if both the degree of hydration (DoH) of BFS increases and there is a sufficiently oxidising environment to convert the released sulfide to sulfate. Prentice et al. [33] found the DoH in Sellafield Ltd specification 3:1 BFS:PC system to be between 50-55% for BFS after one year, with alite and belite hydration at 85% and 53% respectively. There was no intermixing of Calumite® with the GGBS fraction in the Prentice study, and the larger particle size of the Calumite® component will reduce the degree of reaction in the current study; Sanderson et al. found the behaviour of Calumite® to be similar to an inert filler [34]. For the 30 wt% Calumite® replacement in the current study, it is estimated that the DoH is reduced by approximately 10% [35] relative to Prentice et al.

The DoH of the slag has been estimated to be between 40-50% given the level of Calumite® replacement. The clinker hydration has been modelled using the Parrott and Killoh [36] method, after Lothenbach [37]; the degree of hydration of each clinker phase is shown in Table 4.

Table 4 Clinker phases present in anhydrous PC calculated (Taylor-Bogue method [38] *using data from Table 1), and estimated DoH*

Clinker phases	% present in anhydrous PC	% hydrated	Overall DoH
Alite	63.4	81.2	72.3
Belite	16.0	39.7	
Aluminate	7.4	61.2	
Ferrite	7.9	77.9	

The XRF analysis of the anhydrous materials (Table 1) allows the sulfate content of the 3.44:1 BFS:PC system assuming complete oxidation of sulfide to be estimated given different DoH values for the BFS and PC. Given the estimated range of DoH, the concentrations are not anticipated to vary significantly without oxidation of the sulfide (Table 5).

Table 5 Sulfate content of 3.44:1 BFS:PC at varying DoH, with and without the contribution of oxidised sulfide from BFS

		% DoH PC			% DoH PC	
		70	75		70	75
		sulfate (g / 100g solid)	sulfate (g / 100g solid)	+ Sulfide oxidation	sulfate (g / 100g solid)	sulfate (g / 100g solid)
% DoH BFS	40	0.061	0.064		0.233	0.236
	45	0.063	0.066		0.256	0.260
	50	0.065	0.068		0.280	0.283

Thermodynamic modelling of similar systems (unirradiated) [33] predicts ettringite to be replaced by monosulfoaluminate in the phase assemblage by 28 days; monosulfoaluminate and hemicarboaluminate were predicted to be the major AFm components. The persistence of ettringite together with AFm phases can be seen in the XRD data for the BFS:PC control samples (Figure 8), indicating the sulfate had not decreased as predicted. The replacement of ettringite requires a reduction in the SO_3/Al_2O_3 ratio of the system, which occurs as depletion of gypsum and hydration of BFS progresses [11,31,33]. The stability of the AFm phases that are formed upon replacement of the ettringite is also dependent upon the bulk CO_2 content of the system, as the stability of monosulfoaluminate decreases significantly with increasing carbonate contents; the phase assemblage identified by XRD indicates molar bulk ratios of CO_2/Al_2O_3 and SO_3/Al_2O_3 of below 0.5 and between 1-3 respectively [31]. Given the increased carbonation observed in the XRD and TGA results for the PuO_2 samples, the variations in monosulfoaluminate and ettringite may be in part a product of the destabilisation of monosulfoaluminate due to CO_2 increases rather than dramatic sulfate increase.

As can be seen from the above, later age conversion of the AFm phases to ettringite is not only dependent on an increase in sulfate. As the hydrating BFS is assumed to react congruently, the released sulfide is accompanied by Al_2O_3. In terms of oxidation of sulfide, it is considered that this would likely take place as it is released, as radical formation is continuous, rather than remaining as sulfide indefinitely until some mass oxidation event allows conversion to sulfate. Given this, for the complete removal of monosulfoaluminate the Al_2O_3 released would have to be bound into a separate hydrate phase; Taylor et al. summarise several factors that can impact on the Al_2O_3 availability, including the MgO, and CO_2 contents allowing formation of hydrotalcite and carboaluminate phases respectively [11].

It seems unlikely that there would be sufficient sulfate together with the necessary reduction in Al_2O_3 and $CaCO_3$ to allow full conversion of all the monosulfoaluminate to ettringite, however further investigation is required, as this represents a complex set of interactions within a simplified system; the interaction of the waste components in final waste packages is not included here.

TGA results also show variations between the PuO_2 containing and control samples. The initial weight loss between 30-300°C is the result of the loss of free water, C-A-S-H, ettringite, and AFm phases (likely monocarboaluminate(140-180°C) and monosulfoaluminate (180-210°C)). The initial peak at 100°C is typical of cements containing ettringite, and slight broadening of this peak in the PuO_2 containing sample may be due to loss of free water or slight variations in experimental setup [22]. Weight losses at 350-400°C and 400-480°C correspond to the dehydroxylation of hydrotalcite and portlandite respectively, and losses > 500°C are attributed to carbonate decomposition [39].

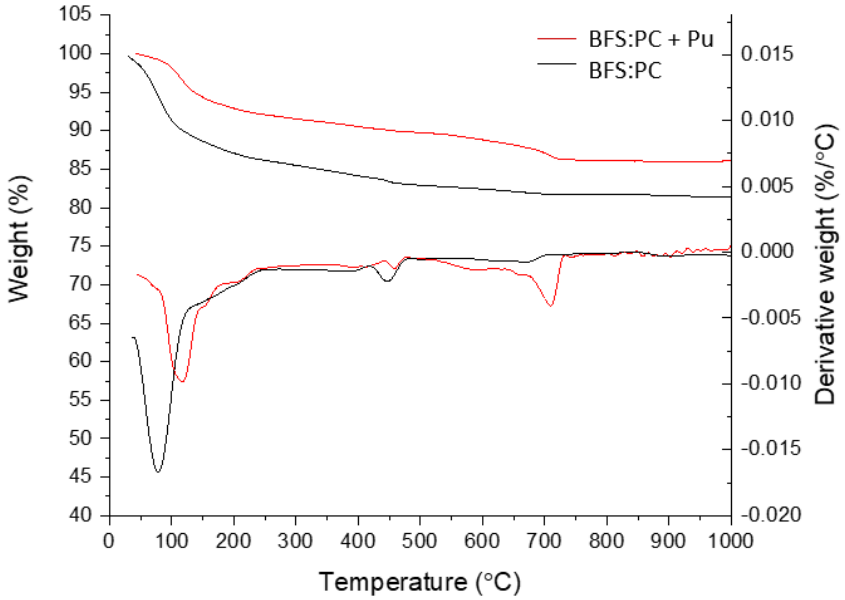

Figure 9 Thermogravimetric analysis of BFS:PC and BFS:PC + Pu

Estimations of free water loss were calculated together with the relative proportions of $Ca(OH)_2$ and $CaCO_3$ for each sample, and the results for all samples are shown in Table 6.

Table 6 Amount of free water loss, $Ca(OH)_2$ and $CaCO_3$ detected by thermogravimetry. Results should be treated tentatively and considered semi-quantitative.

Cement formulation	Free water loss (mass ratio)	$Ca(OH)_2$ (mass ratio)	$CaCO_3$ (mass ratio)
	PuO_2:Control	PuO_2:Control	PuO_2:Control
BFS:PC	0.3 : 1	0.4 : 1	2.4 : 1
PFA:PC	0.3 : 1	-	1.6 : 1
BFS:PC + C	0.5 : 1	0.6 : 1	0.7 : 1
PFA:PC + C	0.3 : 1	-	1.1* : 1

*Data acquisition for this sample is suspected to contain errors at temperatures > 750°C

Greater free water loss was seen in the BFS:PC control sample compared to the BFS:PC + Pu sample, and more $Ca(OH)_2$ remained. Increased weight loss between 500-700°C in the BFS:PC + Pu sample suggests decomposition of mono- and hemi-carbonate species, and may indicate that vaterite / aragonite polymorphs of $CaCO_3$ are present [39–41]. Given the variations in storage conditions between the radioactive and non-radioactive samples in the period between preparation and analysis, atmospheric carbonation effects cannot be fully evaluated and as such the contribution of radiolytic

effects, if any, cannot be ascertained. Increased deposition of aragonite and vaterite in gamma-irradiated Portland cement samples has been linked to an increase in bending strength, as the carbonation maintains the layered C-S-H structure that is disrupted in calcite-carbonation [42]. Further work is required to assess how potential strengthening competes with damage caused through alpha interactions.

3.1.2.1 Effects of cellulose addition

Cellulose addition caused alteration of the proportions of hydrates but no overall changes to the phase assemblage were observed. Peak intensities for ettringite, hydrotalcite and monocarboaluminate increase with cellulose addition, whereas a reduction in the peak intensity for monosulfoaluminate was observed.

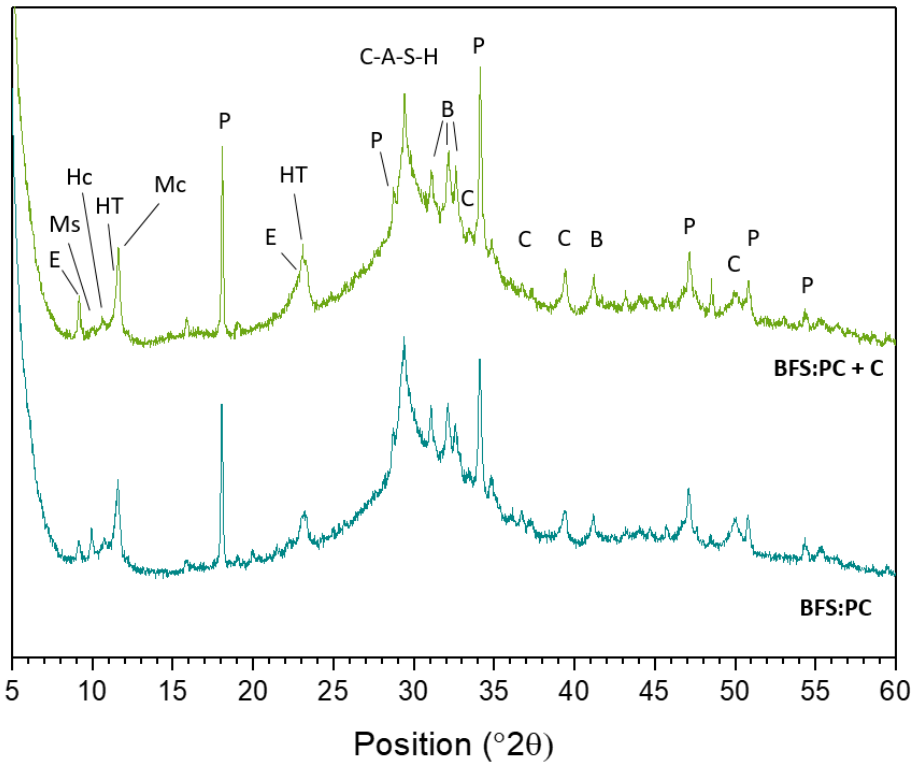

Figure 10 XRD patterns for BFS:PC and BFS:PC + C grouts. E: ettringite, Ms: monosulfoaluminate, Hc: hemicarboaluminate, HT: hydrotalcite, Mc: monocarboaluminate, P: portlandite, C-A-S-H: aluminium substituted calcium silicate hydrate, B: belite, C: calcite

These variations indicate carbonate rich cellulose degradation products influence the phase assemblage, particularly carbonate rich AFm-type phases. The increase in ettringite may be a product of this, as the Al_2O_3 binding to AFm phases will keep the SO_3/Al_2O_3 ratio high [11]. Cellulose degradation does not appear to influence the calcite content, as reflections are similar in both diffractograms. The effects of atmospheric carbonation are considered negligible in all control samples due to the same curing and preparation conditions.

Addition of PuO_2 causes shifts in the proportions of phases present (Figure 11). The loss of free water and $Ca(OH)_2$ are lower in the BFS:PC + C + Pu sample, as seen in the non-cellulose samples (Table 6). The split peak at 100 °C in the PuO_2 containing grout may be a due to loss of free water prior to ettringite dehydration, or a result of the sample size and differences in equipment setup [22]. The weight loss between 300-400°C is indicative of cellulose decomposition [43]. The weight loss observed in the BFS:PC + C + Pu sample at temperatures >550°C is lower than the control sample, indicating less

carbonate products are present. This trend is not observed in any other PuO_2 containing samples, and is surprising as cellulose degradation can lead to increased carbon dioxide formation [19].

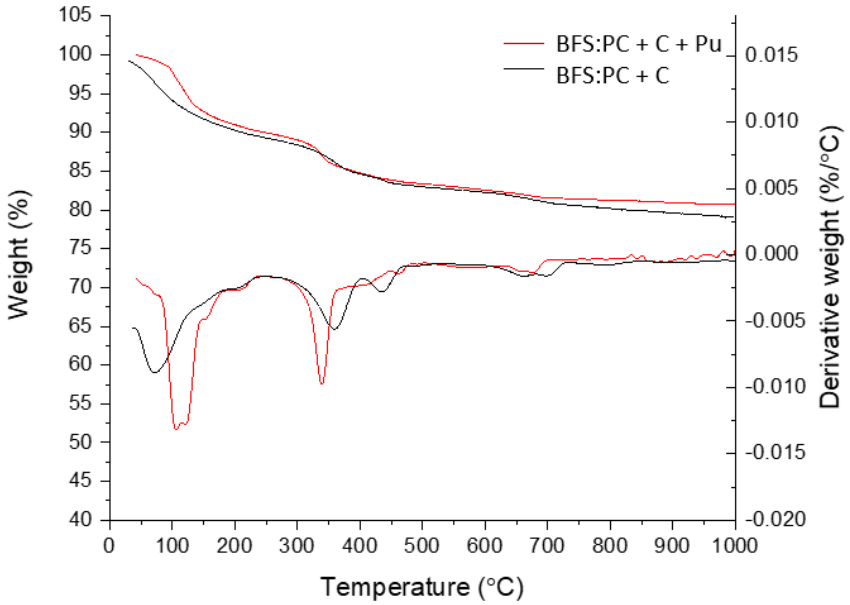

Figure 11. Thermogravimetric analysis of BFS:PC +C and BFS:PC + C + Pu

3.2 Influence of PuO_2 on PFA:PC

3.2.1 Microstructural development

Characteristic microstructures were observed for PFA:PC grouts with textural differences in the matrix indicative of inner and outer product formation during hydration. Unreacted precursor material was identified and no pervasive cracking was observed (Figure 12).

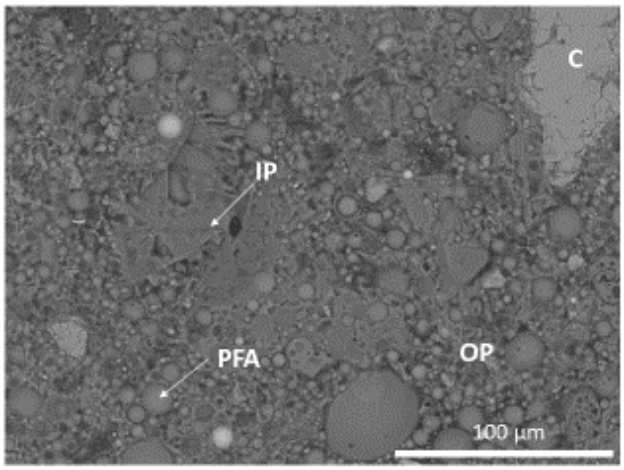

Figure 12 BSE micrographs pf PFA:PC sample. Unhydrated cement clinker: C, unreacted PFA: PFA, matrix inner product: IP, matrix outer product: OP

EDX analysis indicates a hydrated phase assemblage containing C-S-H incorporating Al [44,45] and sulfur containing AFm/AFt phases. Unburnt carbon particles from the PFA were observed as darker zones in the matrix (Figure 13). Minor alteration was observed on surface of some PFA particles; aluminium enrichment and dendritic features were identified. These dendritic features may represent mullite crystals that are exposed as the hydration of the glass phase of the PFA consumes the particle

[46,47]. The matrix texture appears slightly less dense than in the BFS:PC samples, which could be the result of the slower rate of reaction of PFA in PC blends [44].

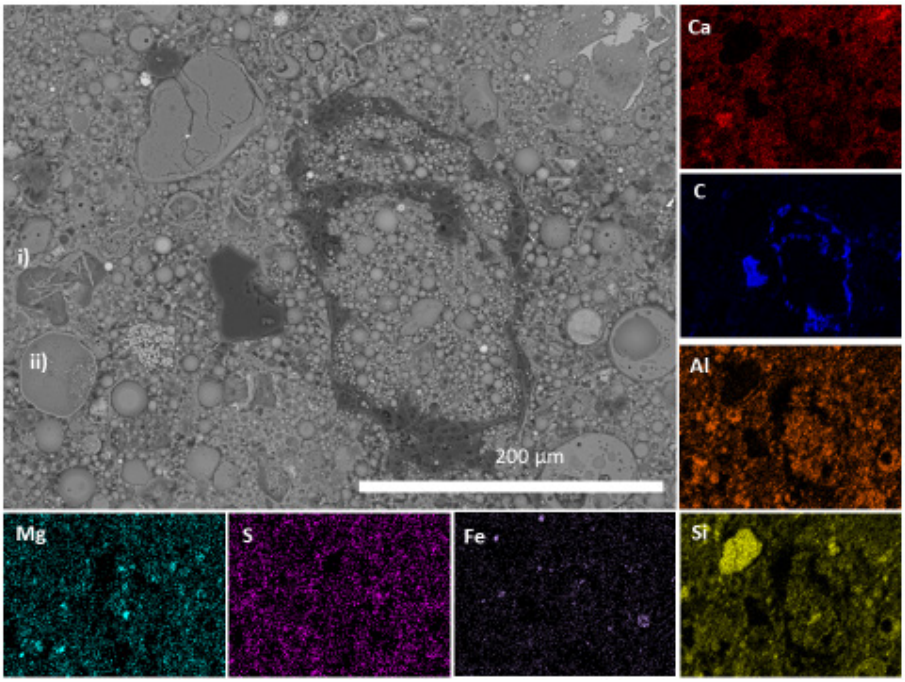

Figure 13 BSE micrograph and EDX analysis of PFA:PC showing unburnt carbon particle. Label i) shows ettringite needle formation, and ii) Al enriched PFA rim.

The PFA:PC + Pu samples displayed similar textures, and the PuO_2 does not appear to have significantly impacted the matrix. Optical investigation indicated no pervasive deformation of the bulk, with no large cracks identified (Figure 14).

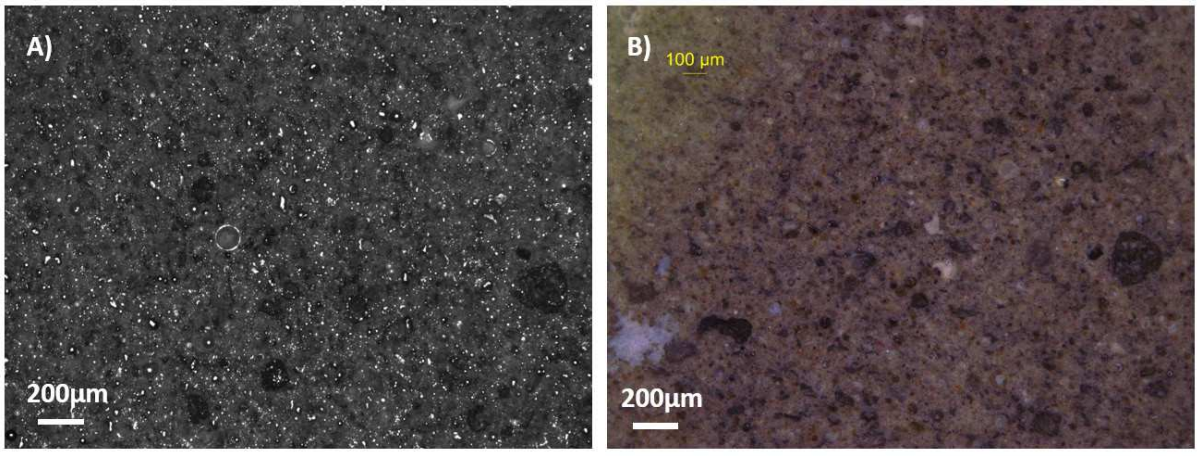

Figure 14 Optical images of PFA:PC + Pu. A) Dark field image, B) Bright field image

SEM analysis of PFA:PC + Pu (Figure 15) also indicates there is smaller scale cracking, and the PuO_2 particles are well encapsulated albeit with less intimate contact to the grout than seen in the BFS samples (Figure 7, section 3.1.1). This effect is exaggerated in Figure 15 B) due to the high contrast PuO_2 particle; the dark areas adjacent to the particle are likely low contrast hydrate products.

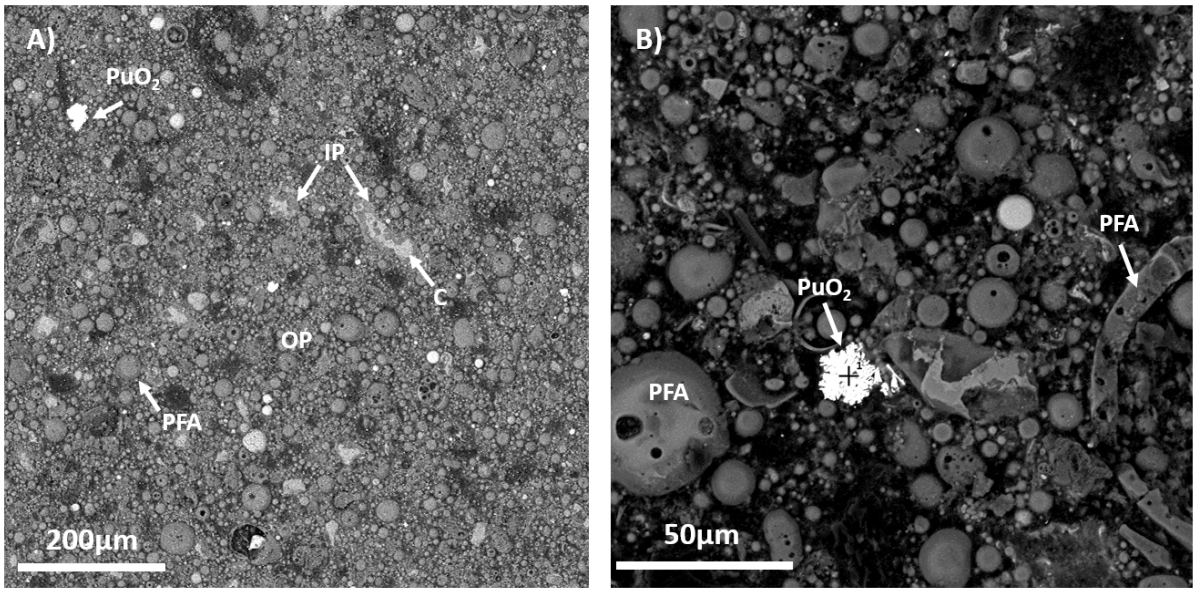

Figure 15 BSE images of PFA:PC + Pu at increasing magnification. Unhydrated cement clinker: C, unreacted PFA: PFA, matrix inner product: IP, matrix outer product: OP

3.2.1.1 Effects of cellulose addition

The cellulose powder appears well encapsulated in the PFA:PC + C samples with limited impact on the microstructural development. The phase assemblage is as identified in the PFA:PC grout, with similar textural development observed. Some dehydration of the cellulose is apparent, with cracking and shrinkage away from the grout encapsulant (Figure 16).

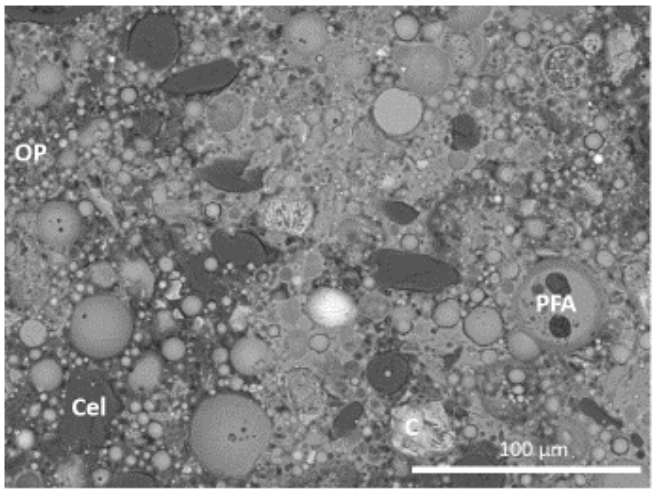

Figure 16 BSE micrograph of PFA:PC + C grouts showing encapsulation of cellulose powder in the matrix. Cel: cellulose powder, PFA: unreacted PFA, OP: matrix outer product.

PuO_2 addition does not appear to significantly affect the microstructure, with no pervasive cracking noted in PFA:PC + C + Pu samples (Figure 17). Optical images show a dense microstructure, with identifiable unburnt carbon particles and PFA in the hydrate matrix. Porosity was estimated at 2.9% using thresholding of the greyscale histogram. Zones of red brown colouration similar to those identified in the BFS:PC blends are present, together with highly reflective white regions; these may represent zones of unhydrated PC or PFA agglomerations within the matrix (Figure 14 B).

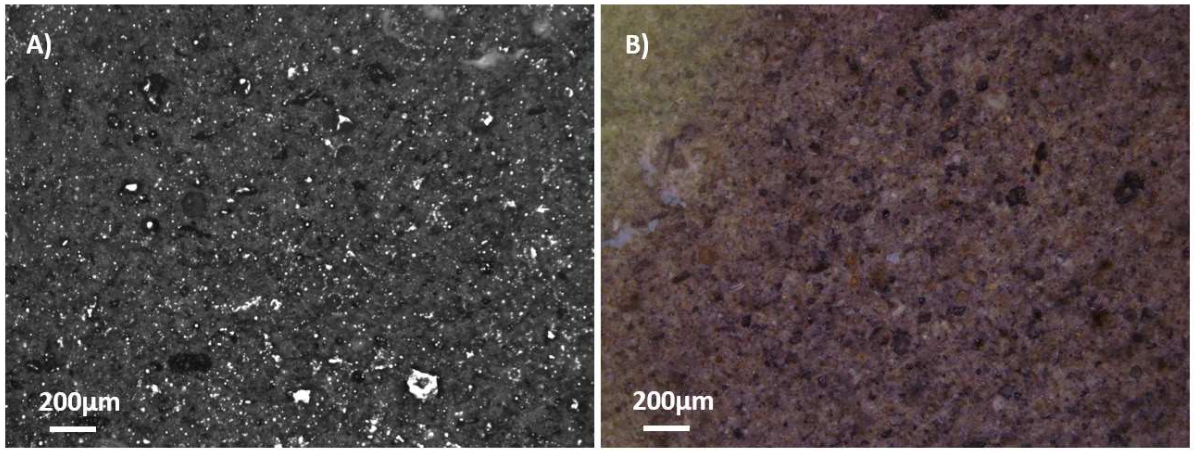

Figure 17 Optical images of PFA:PC + C + Pu cements. A) Dark field image, B) Bright field image

3.2.2 Phase assemblage

The PFA:PC materials contained strätlingite (PDF#-29-0285), mullite (PDF#-79-1453), and quartz (PDF#-85-0335) in addition to several phases identified in the BFS containing blend (Figure 18).

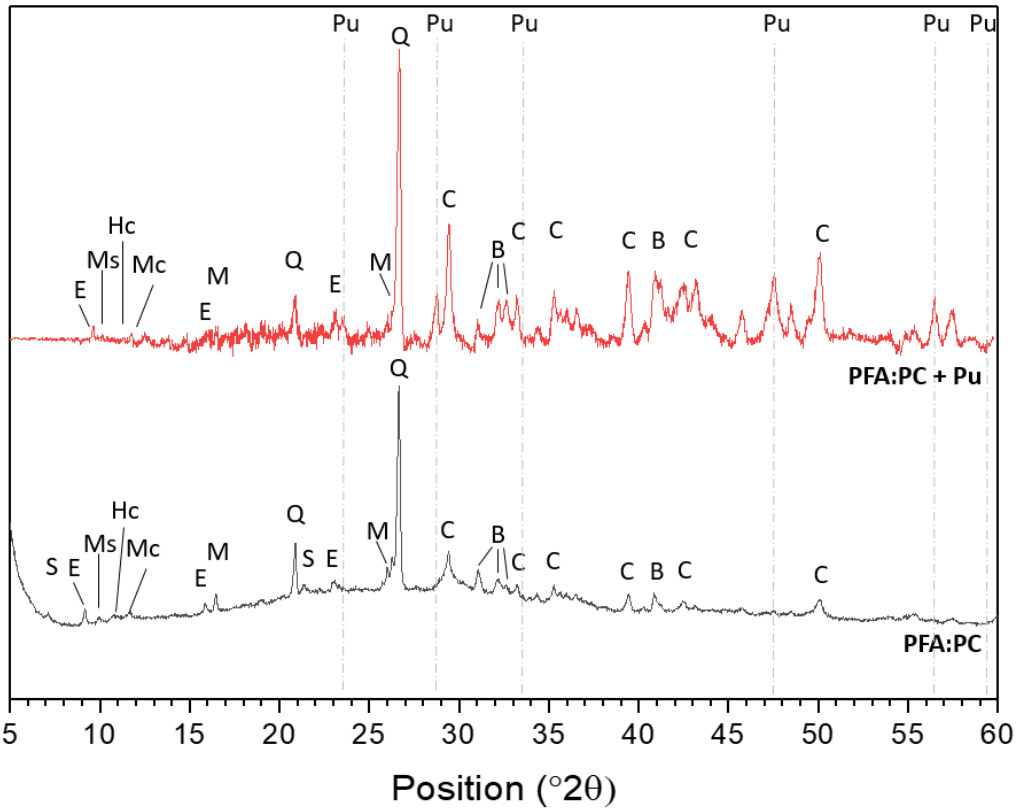

Figure 18 XRD data from PFA:PC and PFA:PC + Pu grouts. S: strätlingite, E: ettringite, Ms: monosulfoaluminate, Hc: hemicarboaluminate, Mc: monocarboaluminate, M: mullite, Q: quartz, B: belite, C: calcite, Pu: PuO_2.

The shift in peak position for the [100] ettringite reflection was observed in the PFA:PC + Pu sample (discussed in section 3.1.2), however no significant alteration in the peak intensity was noted. The monosulfoaluminate reflection is not present in the PFA:PC + Pu diffractogram, indicating potential destabilisation of monosulfoaluminate. However, no formation of other sulfate containing phases is noted, and so it is considered a result of the background stripping applied to the data. Strong reflections for calcite are observed in the PFA:PC + Pu sample, and TGA results (Figure 19) also show a higher proportion of carbonates (Table 6, section 3.1.2). Increased weight loss between 500-700°C

was noted with a smaller peak centred at 730°C, indicating a range of carbonate species were present as discussed in section 3.1.2. Weight losses indicative of ettringite and AFm are also observed. The weight loss <100°C is reduced in the PFA control blends comparative to the BFS controls, likely a result of fewer AFm phases undergoing dehydration in this formulation together with a smaller weight loss contribution from free water.

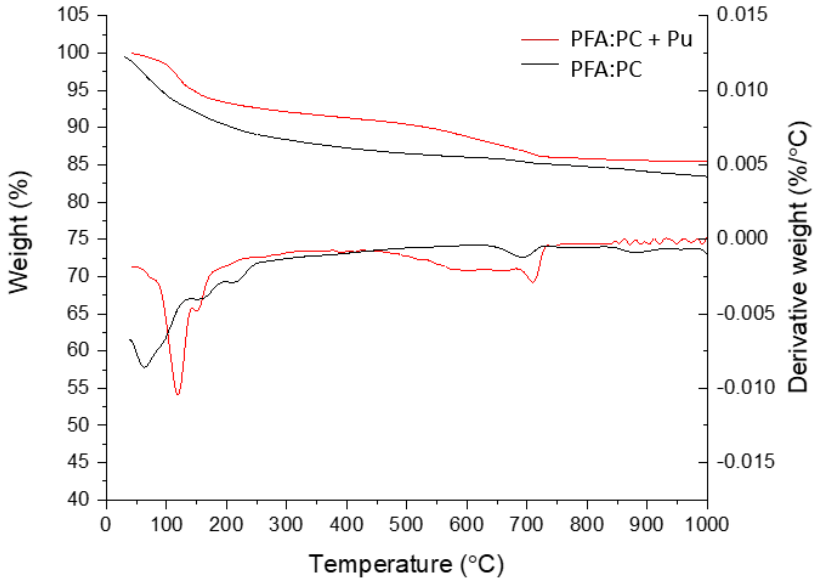

Figure 19. Thermogravimetric analysis of PFA:PC and PFA:PC + Pu.

3.2.2.1 Effects of cellulose addition

Cellulose addition caused similar variation to those seen in the BFS systems. Peak intensities for ettringite, hemicarbonate and monocarboaluminate increased in the cellulose containing sample (Figure 20), whilst the reflection for monosulfoaluminate at 9.9°2θ reduced.

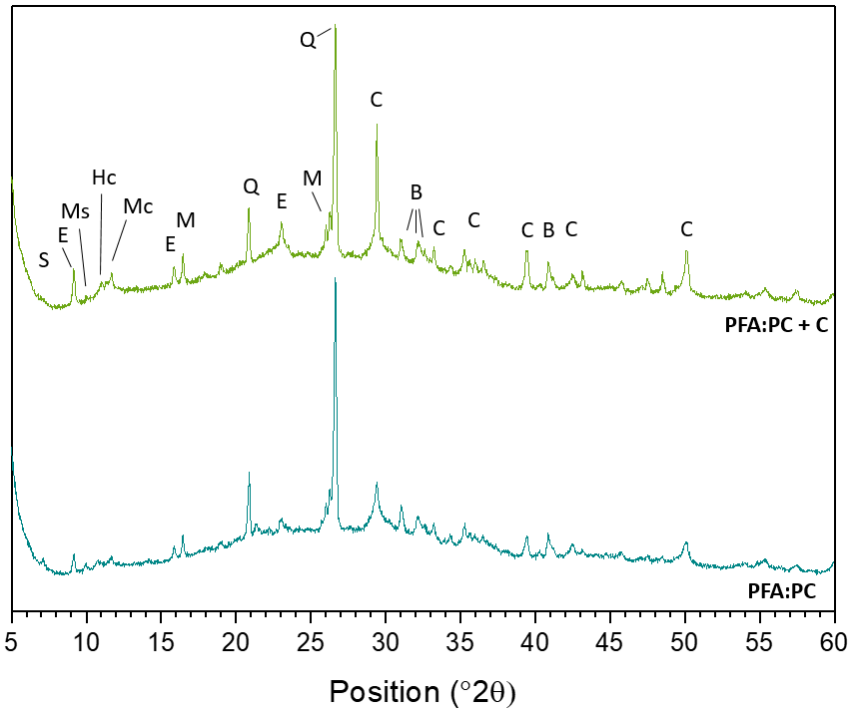

Figure 20. XRD data for PFA:PC and PFA:PC + C grouts. S: strätlingite, E: ettringite, Ms: monosulfoaluminate, Hc: hemicarboaluminate, Mc: monocarboaluminate, M: mullite, Q: quartz, B: belite, C: calcite.

The increase in hemi- and monocarboaluminate indicates higher carbonate contents in the PFA:PC + C sample; this is likely due to the degradation of cellulose, as atmospheric carbonation effects are expected to be limited (see section 3.2.3). However, the peak intensities for calcite appear increased in the PFA:PC + C diffraction pattern suggesting the cellulose degradation products could not be accommodated through formation of additional AFm type phases. TGA results support the increase in AFm-type phases (Figure 21). Weight loss between 300-400°C indicates decomposition of cellulose, which was greater in the PFA sample than observed in section 3.1.2.1.

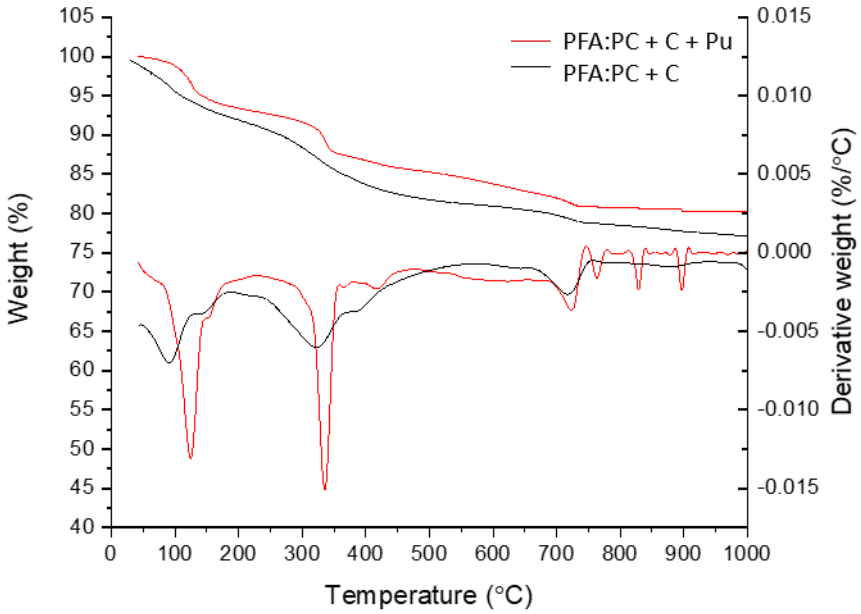

Figure 21 Thermogravimetric analysis of PFA:PC + C and PFA:PC + C + Pu. Data acquisition of PFA:PC + C + Pu suspect at T > 750°C.

The PFA:PC + C + Pu sample shows increased weight loss at temperatures >500°C, suggesting increased carbonation in the PFA system which may be linked to an increase in cellulose degradation products; however, the data becomes unreliable at temperatures >750°C and so further investigation is required.

4. Gas evolution results and discussion

4.1 Gas evolution results

Figure 22 shows PuO_2 containing samples in a glass vessel prior to hydrogen yield measurement.

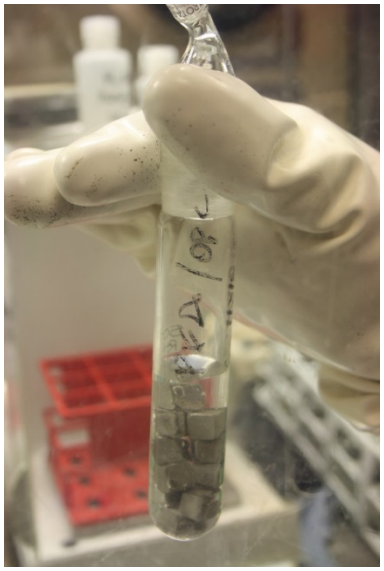

Figure 22 Photograph of PFA/PC+C samples in glass vessel as used for hydrogen yield measurement.

Hydrogen radiation chemical yields are summarised in Table 7, based on the total energy absorbed by the cement. Hydrogen production rates were linear with time and repeat measurements on each sample were generally within ±0.1 molecules.100eV^{-1} of the mean.

Table 7 Hydrogen yields from α-self irradiation of PuO_2-containing cement (1 cm^3 sample)

Cement formulation	Mean G(H_2) (molecules.100eV^{-1})
BFS:PC + Pu	0.37
BFS:PC + C + Pu	0.60
PFA:PC + Pu	0.33
PFA:PC + C + Pu	0.91

Hydrogen yields from the BFS:PC + Pu and PFA:PC + Pu were similar, falling in the same range, whilst hydrogen yields from cellulose containing samples (BFS:PC + C + Pu and PFA:PC + C + Pu) were consistently higher.

4.2 Gas evolution discussion

The hydrogen yield from an ~5 MeV α-particle of helium ion irradiation in water is G(H_2) = 1.2-1.3 molecules.100 eV^{-1} [48–50]. The current experiments use PuO_2 as the radiation source and therefore some energy will be absorbed by the PuO_2 lattice itself as well as by unhydrated cement phases and will not contribute to hydrogen production. Figure 23 shows SEM images of PuO_2 particles from the batch of oxide used in the current experiments and shows particles are typically 20-40 µm in diameter. The range of a 5.5 MeV α-particle through the PuO_2 lattice is 12.5 µm, but since the PuO_2 particles are highly porous and formed from an agglomeration of much smaller crystallites, the density of particles is probably about 50 % crystalline density and the effective range is therefore greater. Thus, the particle dimensions are a significant fraction of the particle range and a significant fraction of energy will be absorbed by the PuO_2.

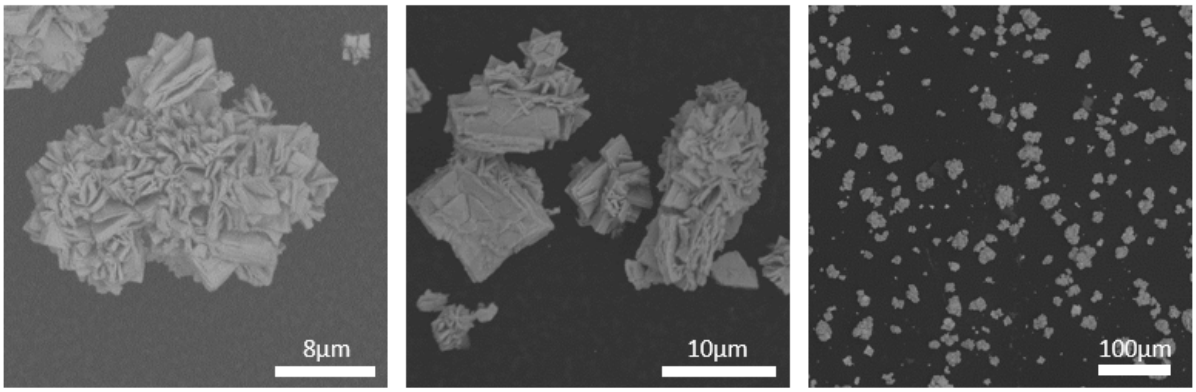

Figure 23 SEM images of Magnox PuO_2 powder used in this investigation

A practical estimate of the energy self-absorbed by PuO_2 can be made from measurements of the hydrogen yield from a slurry of Magnox PuO_2 in aqueous sodium nitrite that was measured to be $G(H_2)$ = 0.63 molecules.100 eV^{-1} [51]; sodium nitrite was used to scavenge OH to prevent it reacting with H_2, although this is not a large effect under α-irradiation. This suggests that on average about 50 % of the α-particle energy is absorbed by the PuO_2. This is consistent with calculated estimates assuming spherical particles with diameter ~30 µm [52]. It follows that $G(H_2)$ is not expected to exceed ~0.6 molecules.100 eV^{-1} from cement, unless energy transfer from the oxides in the cement matrix occurs.

In addition to absorption of energy by the PuO_2, the hydrogen yields from cement will depend on the fraction of α-particle energy escaping from the PuO_2 particles that is absorbed by unhydrated components and by water in the cement matrix as either structural or pore water. The latter is expected to be determined mainly by the volume fraction of water in the matrix. This has been reported in recent gamma irradiation studies where the hydrogen yield from structural water in the hydrated phases and pore water was found to be fairly similar to the yield from bulk water [53]. In the present case it is not straight forward to accurately estimate the dose to water within the matrix owing to heterogeneity on the length scale of the alpha particle of hydrated and unhydrated components in the matrix. In addition, the dose must take into account differences in the stopping power of the different components. Consequently a detailed comparison of the hydrogen yield from water in the matrix cannot be made with the expected value for bulk water. It is possible that additional water may have been absorbed under saturated storage conditions, increasing the overall water content from the 26-30 wt% used in the mix. Also, hydrated phases will tend to infill the immediate vicinity around PuO_2 particles and increase the local water content. Given this, measured yields appear reasonably consistent with expectations based on bulk water yields and self-absorption by the PuO_2.

Only a handful of measurements of hydrogen yields from alpha radiolysis of cements have been reported in the open literature. Bibler reported values $G(H_2)$=0.63 molecules 100 ev^{-1} for an OPC/gypsum cement w/s=0.7 [54]. Curium was dissolved in the pore water so that self-absorption of the radiation would not have occurred, probably accounting in the higher yield than measured in the present study. Crapse et al. reported hydrogen yields from a cement sample (unspecified composition) containing 1wt % PuO_2 and 16.5 wt% water to be 0.15 molecules 100 ev^{-1} [55]. The lower yield compared with the results reported here is probably a consequence of the much lower water content.

Samples containing cellulose gave consistently substantially higher hydrogen yields. This is surprising considering the relatively low mass fraction of cellulose in the formulation. This is presumably, in part, because the hydrogen yield of cellulose is significantly higher than for cement. The hydrogen yield from alpha irradiation of cellulose has been reported to have an initial value of approximately

G(Gas)=1.5-1.9 molecules.100eV^{-1} and ~60% H_2 giving a hydrogen yield of G(H_2)= 0.9-1.1 molecules.100eV^{-1} [56]. Similar results in a Los Alamos National Laboratory report gave initial G(gas)~1.5 molecules.100eV^{-1} and ~50% H_2 giving a hydrogen yield of G(H_2)=0.75 molecules.100eV^{-1} [57]. In both cases, these measurements were made by contaminating the surface of the test material with PuO_2 without accounting for self-absorption of energy by the PuO_2, and therefore these studies underestimate the true yield, which should be significantly greater in magnitude than for bulk water. This means that where cellulose particles are in close proximity to PuO_2 the hydrogen yield from the cellulose will be much greater than the cement it has displaced. Absorption of water by the cellulose may further enhance the yield by swelling the volume occupied by cellulose and the fraction of radiation absorbed by water. However, it currently remains difficult to quantitatively explain the much greater yield for the cellulose containing samples. A detailed analysis would require a more complete understanding of the distribution of cellulose and water, and calculation of the dose to cellulose in the matrix.

5. Conclusions

This study provides novel investigation of how PuO_2 encapsulation affects the physico-chemical development of Portland cement blended grouts typically used for waste management in the UK. Many waste streams include alpha emitting species, which will result in extremely localised radiation fields in regions immediately surrounding the alpha source – a situation that cannot be simulated by external gamma radiation. PuO_2 is a particularly intense alpha emitter, and since no UK waste stream currently incorporates particulate PuO_2 at the levels used here, the experiments represent a worst case as regards alpha radiolysis effects on immobilised UK ILW.

Grout formulations and cement/SCM powders used in the experiments are identical to those used in the UK nuclear industry, and the PuO_2 used had relevant morphology, mineralogy and isotopic composition. Mixing processes aimed to simulate encapsulation plant processes as closely as practicable.

Several UK waste streams include organics which historically included sources of cellulose. The inclusion of high levels of cellulose in powder form allowed intimate intermixing between the grout and cellulose, producing samples that represent an unrealistic worst case scenario unlikely to be encountered in UK waste streams.

Microscopic analysis indicates there is good physical contact between cement hydrates and PuO_2 particle agglomerates, with evidence of some infilling between particles. No microstructural damage to the cement hydrates was observed, even in the regions closest to the PuO_2 particle agglomerates. The mineralogy and morphology of the PuO_2 appears unchanged by contact with cementitious grouts, however limited EDX of the active samples was completed so no information is available on Pu mobility or whether it has been incorporated in hydrate phases. Further characterisation is recommended, particularly focussing on the interface between the PuO_2 particle agglomerates and the encapsulant grouts. The evidence available from this study indicates that Portland cement blends are suitable encapsulating matrices for wastes containing PuO_2 (whether in this physical form or as a component of other waste streams arising from spent fuel reprocessing).

XRD and TGA results indicate phase assemblages characteristic of the blended cements investigated; no significant crystal reflections for new hydrate phases in XRD were observed, and no additional weight loss was seen at temperature ranges inconsistent with these blends. Incorporation of cellulose caused variation in the proportion of phases present, likely due to cellulose degradation, but no microstructural differences were observed.

Comparison of the PuO_2 samples with the controls suggests quantitative differences in the phase assemblage. The ratio of sulfate phases in the BFS blends appear to have altered in the presence of PuO_2, with an increase in ettringite observed. This change may be driven by a combination of factors, including an increase in the CO_2/Al_2O_3 ratio. Despite conversion of monosulfoaluminate to ettringite being linked with structural damage in sulfate attacked concretes, no evidence of structural damage was apparent in these small scale samples. The potential radiolytic oxidation of sulfide released through hydration of BFS increasing the sulfate content is considered insufficient to cause significant structural issues, as the bulk SO_3/Al_2O_3 ratio will be buffered by the alumina also released from the BFS. Further work is needed to assess the extent of chemical variations in the area surrounding the PuO_2 agglomerate particles with regard to the sulfate phase ratio, and how the carbonate content affects the AFm phase balance in these areas.

Differences in amount of carbonates present were observed, however due to the different storage and handling of the radioactive samples and controls this cannot be attributed to radiation effects. Although the results indicate that radiolytic carbonation may have occurred, no systematic trends were observed for the different samples analysed.

Gas evolution data for the samples show slightly elevated $G(H_2)$ values compared to those in literature for similar systems, which is thought to be a product of the idealised curing condition used in the current study. Results are consistent with what would be expected based on the likely radiation deposition, taking account of self-absorption within the PuO_2 particle agglomerates. The addition of cellulose increased the $G(H_2)$ values in all samples; this is probably due to the contribution of cellulose radiolysis products and additional water absorption by the cellulose creating an enhanced water content in the samples.

Acknowledgements

The authors wish to acknowledge the and Engineering and Physical Sciences Research Council (EPSRC) who funded the research activity carried out by the University of Sheffield via the Next Generation Nuclear Centre for Doctoral Training together with the DISTINCTIVE University Consortium and UK NDA for sponsorship of the project. This research was performed in part at the MIDAS Facility, at the University of Sheffield, which was established with support from the Department of Energy and Climate Change. The authors wish to also acknowledge the investment made by NNL to fund its collaborative research for this project, made possible by earnings reinvested in the NNL Core Science programme.

References

[1] Nuclear Decommissioning Authority, Radioactive Wastes in the UK: A Summary of the 2016 inventory, 2016.

[2] Radioactive Waste Management, Packaging of Plutonium Contaminated Material at the Waste Treatment Complex (Extension to Final stage and Periodic Review) Summary of Assessment Report, 2008.

[3] Nuclear Decommissioning Authority, Waste Stream 2D03 Plutonium Contaminated Material; Drums, 2016.

[4] Nuclear Decommissioning Authority, Waste Stream 2D24: Magnox Cladding and Miscellaneous Solid Waste, 2013.

[5] Nuclear Decommissioning Authority, Waste Stream 2D22: Magnox Cladding and Miscellaneous Solid Waste, 2013.

627 [6] J.W. Spinks, R. Woods, An introduction to radiation chemistry, 2nd edition, Wiley, New York,
628 1976.

629 [7] Nuclear Decommissioning Authority, Waste Package Specification and Guidance
630 Documentation, WPS/800: Wasteform Specification for 500 litre Drum waste Package:
631 Explanatory Material and Design Guidelines, 2008.

632 [8] F.P. Glasser, Cements in radioactive waste disposal, MRS Bull. 19 (1994) 33–38.

633 [9] I.G. Richardson, G.W. Groves, C.R. Wilding, Effect of gamma radiation on the microstructure
634 and microchemistry of GGBFS/OPC cement blends, MRS Proc. 176 (1990) 31–37.

635 [10] H. Christensen, E. Bjergbakke, SKBF KBS Technical Report 84-02: Radiolysis of concrete, 1984.

636 [11] H.F.W. Taylor, C. Famy, K.L. Scrivener, Delayed ettringite formation, Cem. Concr. Res. 31 (2001)
637 683–693.

638 [12] M. Whittaker, M. Zajac, M. Ben Haha, L. Black, The impact of alumina availability on sulfate
639 resistance of slag composite cements, Constr. Build. Mater. 119 (2016) 356–369.

640 [13] Radioactive Waste Management, Nuclear Decommissioning Authority, Geological Disposal:
641 Waste Package Evolution Status Report, 2016.

642 [14] T.M. Rosseel, I. Maruyama, Y. Le Pape, O. Kontani, A.B. Giorla, I. Remec, J.J. Wall, M. Sircar, C.
643 Andrade, M. Ordonez, Review of the current state of knowledge on the effects of radiation on
644 concrete, J. Adv. Concr. Technol. 14 (2016) 368–383.

645 [15] R.V. Gentry, Giant radioactive halos: indicators of unknown radioactivity?, Science 169 (1970)
646 670–673.

647 [16] R.V. Gentry, Fossil alpha-recoil analysis of certain variant radioactive halos, Science 160 (1968)
648 1228–1230.

649 [17] W.R. Bower, R.A.D. Pattrick, C.I. Pearce, G.T.R. Droop, S.J. Haigh, Radiation damage haloes in
650 biotite investigated using high-resolution transmission electron microscopy, Am. Mineral. 101
651 (2016) 105–110.

652 [18] W.R. Bower, C.I. Pearce, G.T.R. Droop, J.F.W. Mosselmans, K. Geraki, R.A.D. Pattrick, Radiation
653 damage from long-term alpha particle bombardment of silicates – a microfocus XRD and Fe K-
654 edge XANES study, Mineral. Mag. 79 (2015) 1455–1466.

655 [19] P.N. Humphreys, A. Laws, J. Dawson, A Review of Cellulose Degradation and the Fate of
656 Degradation Products Under Repository Conditions. Technical Report, Nuclear
657 Decommissioning Authority (NDA), UK. 2010.

658 [20] I. Pavasars, J. Hagberg, H. Borén, B. Allard, Alkaline degradation of cellulose: mechanisms and
659 kinetics, J. Polym. Environ. 11 (2003) 39–47.

660 [21] M.J. Angus, I.H. Godfrey, M. Hayes, S. Foster, Managing change in the supply of cement
661 powders for radioactive waste encapsulation – twenty years of operational experience, Waste
662 Management Conference Proceedings, Phoenix, AZ (2010).

663 [22] K. Scrivener, R. Snellings, B. Lothenbach, A Practical Guide to Microstructural Analysis of
664 Cementitious Materials, 1st ed., Taylor & Francis Group, 2016.

665 [23] B. Lothenbach, P. Durdziński, K. De Weerdt, Thermogravimetric Analysis, in: A Practical Guide
666 to Microstructural Analysis of Cementitious Materials, 2016: pp. 177–212.

667 [24] A.S. Lubansky, Y.L. Yeow, Y.-K. Leong, S.R. Wickramasinghe, B. Han, A general method of

668 computing the derivative of experimental data, AIChE J. 52 (2006) 323–332.

669 [25] J. Hill, J.H. Sharp, The mineralogy and microstructure of three composite cements with high
670 replacement levels, Cem. Concr. Compos. 24 (2002) 191–199.

671 [26] E. L'Hôpital, B. Lothenbach, G. Le Saout, D. Kulik, K. Scrivener, Incorporation of aluminium in
672 calcium-silicate-hydrates, Cem. Concr. Res. 75 (2015) 91–103.

673 [27] M. Whittaker, M. Zajac, M. Ben Haha, F. Bullerjahn, L. Black, The role of the alumina content
674 of slag, plus the presence of additional sulfate on the hydration and microstructure of Portland
675 cement-slag blends, Cem. Concr. Res. 66 (2014) 91–101.

676 [28] R. Snellings, T. Paulhiac, K. Scrivener, The effect of Mg on slag reactivity in blended cements,
677 Waste Biomass Valoriz. 5 (2014) 369–383.

678 [29] S.A. Bernal, V. Rose, J.L. Provis, The fate of iron in blast furnace slag particles during alkali-
679 activation, Mater. Chem. Phys. 146 (2014) 1–5.

680 [30] G. Möschner, B. Lothenbach, F. Winnefeld, A. Ulrich, R. Figi, R. Kretzschmar, Solid solution
681 between Al-ettringite and Fe-ettringite ($Ca_6[Al_{1-x}Fe_x(OH)_6]_2(SO_4)_3 \cdot 26H_2O$), Cem. Concr. Res. 39
682 (2009) 482–489.

683 [31] T. Matschei, B. Lothenbach, F.P. Glasser, The AFm phase in Portland cement, Cem. Concr. Res.
684 37 (2007) 118–130.

685 [32] V. Ramachandran, R.M. Paroli, J.J. Beaudoin, A.H. Delgado, Handbook of Thermal Analysis of
686 Construction Materials, 2002.

687 [33] D.P. Prentice, S.A. Bernal, M. Bankhead, M. Hayes, J.L. Provis, Phase evolution of slag-rich
688 cementitious grouts for immobilisation of nuclear wastes: an experimental and modelling
689 approach, Adv. Cem. Res. 30 (2017) 1–46.

690 [34] R.A. Sanderson, J.L. Provis, G.M. Cann, The effect of blast-furnace slag particle size on the
691 hydration of slag – Portland cement grouts at elevated temperatures, Adv. Cem. Res. 30 (2018)
692 337–344.

693 [35] R.A. Sanderson, G.M. Cann, J.L. Provis, Comparison of calorimetric methods for the assessment
694 of slag cement hydration, Adv. Appl. Ceram. 116 (2017) 186–192.

695 [36] L.J. Parrot, D.C. Killoh, Prediction of cement hydration, Br Ceram Proc. 35 (1984) 41-53.

696 [37] B. Lothenbach, T. Matschei, G. Möschner, F.P. Glasser, Thermodynamic modelling of the effect
697 of temperature on the hydration and porosity of Portland cement, Cem. Concr. Res. 38 (2008)
698 1–18.

699 [38] H.F.W. Taylor, Modification of the Bogue calculation, Adv. Cem. Res. 2 (1989) 73–77.

700 [39] N.C. Collier, Transition and decomposition temperatures of cement phases - a collection of
701 thermal analysis data, Ceram.-Silik. 60 (2016) 1–10.

702 [40] B. Wu, G. Ye, Development of porosity of cement paste blended with supplementary
703 cementitious materials after carbonation, Constr. Build. Mater. 145 (2017) 52–61.

704 [41] I. Maruyama, S. Ishikawa, J. Yasukouchi, S. Sawada, R. Kurihara, M. Takizawa, O. Kontani,
705 Impact of gamma-ray irradiation on hardened white Portland cement pastes exposed to
706 atmosphere, Cem. Concr. Res. 108 (2018) 59–71.

707 [42] I. Maruyama, O. Kontani, M. Takizawa, S. Sawada, S. Ishikawao, J. Yasukouchi, O. Sato, J. Etoh,
708 T. Igari, Development of soundness assessment procedure for concrete members affected by

neutron and gamma-ray irradiation, J. Adv. Concr. Technol. 15 (2017) 440–523.

[43] H. Yang, R. Yan, H. Chen, D.H. Lee, C. Zheng, Characteristics of hemicellulose, cellulose and lignin pyrolysis, Fuel. 86 (2007) 1781–1788.

[44] B. Lothenbach, K. Scrivener, R.D. Hooton, Supplementary cementitious materials, Cem. Concr. Res. 41 (2011) 1244–1256.

[45] F. Deschner, F. Winnefeld, B. Lothenbach, S. Seufert, P. Schwesig, S. Dittrich, F. Goetz-Neunhoeffer, J. Neubauer, Hydration of Portland cement with high replacement by siliceous fly ash, Cem. Concr. Res. 42 (2012) 1389–1400.

[46] R.R. Lloyd, J.L. Provis, J.S.J. Van Deventer, Microscopy and microanalysis of inorganic polymer cements. 1: Remnant fly ash particles, J. Mater. Sci. 44 (2009) 608–619.

[47] P.T. Durdziński, Hydration of multi-component cements containing cement clinker , slag , calcareous fly ash and limestone, Thesis no. 6834, EPFL, 2016.

[48] N.E. Bibler, Curium-244 α radiolysis of nitric acid. Oxygen production from direct radiolysis of nitrate ions, J. Phys. Chem. 78 (1974) 211–215.

[49] W.. Burns, H.. Sims, Effect of radiation type in water radiolysis, J. Chem. Soc. Faraday Trans. 1 Phys. Chem. Condens. Phases. 77 (1981) 2803–2813.

[50] C.R. Gregson, G.P. Horne, R.M. Orr, S.M. Pimblott, H.E. Sims, R.J. Taylor, K.J. Webb, Molecular hydrogen yields from the α-self-radiolysis of nitric acid solutions containing plutonium or americium, J. Phys. Chem. B. 122 (2018) 2627–2634.

[51] H. Sims, K.J. Webb, J. Brown, D. Morris, R.J. Taylor, Hydrogen yields from water on the surface of plutonium dioxide, J. Nucl. Mater. 437 (2013) 359–364.

[52] U.S. Nuclear Regulatory Commission, RH-TRU payload appendices Revision 1, 2011.

[53] D. Chartier, J. Sanchez-Canet, L. Bessette, S. Esnouf, J.P. Renault, Influence of formulation parameters of cement based materials towards gas production under gamma irradiation, J. Nucl. Mater. 511 (2018) 183–190.

[54] N.E. Bibler, M.L. Hyder, Radiolytic Gas Production From Concrete Containing Savannah River Plant Waste, 1978.

[55] K. Crapse, C.A. Langton, J.M. Duffey, L.N. Oji, C.L. Crawford, Updated G-values and radiolysis data for hydrated waste forms containing alpha oxide, in: 41st Actinides Separation Conference, Argonne, Illinois, 2017.

[56] S.T. Kosiewicz, Gas generation from organic transuranic wastes. I. Alpha radiolysis at atmospheric pressure, Nucl. Technol. 54 (1981) 92–99.

[57] A. Zerwekh, Gas generation from radiolytic attack of TRU-contaminated hydrogenous waste, Los Alamos Natl. Lab. Rep. LA-7674-MS (1979).